



Speeding up CFD simulation of fluidized bed reactor for MTO by coupling CRE model



Bona Lu ^a, Hao Luo ^{a,b}, Hua Li ^c, Wei Wang ^{a,*}, Mao Ye ^{c,*}, Zhongmin Liu ^c, Jinghai Li ^a

^a State Key Laboratory of Multiphase Complex Systems, Institute of Process Engineering, Chinese Academy of Sciences, Beijing 100190, China

^b University of Chinese Academy of Sciences, Beijing 10049, China

^c Dalian National Laboratory for Clean Energy, National Engineering Laboratory for MTO, Dalian Institute of Chemical Physics, Chinese Academy of Sciences, Dalian 116023, China

HIGHLIGHTS

- CSTR model is used to initialize species distribution for CFD simulation.
- CRE-based initialization shortens the unsteady process for reactive flow modeling.
- EMMS/bubbling drag allows reasonable prediction of fluidized bed expansion.

ARTICLE INFO

Article history:

Received 18 September 2015

Received in revised form

1 December 2015

Accepted 11 January 2016

Available online 18 January 2016

Keywords:

CRE

CFD

Methanol-to-olefins (MTO)

EMMS

Kinetics

Fluidized bed

ABSTRACT

The methanol to olefins (MTO) process opens an economical and important route to produce light olefins. The design of MTO reactor borrows ideas from the reaction–regeneration configuration of the modern fluid catalytic cracking (FCC) units. However, their hydrodynamic behaviors are quite different in the sense that the fluidized bed for MTO reactions operates in different flow regime from that of FCC, calling for new modeling for scale-up. In addition, the coke deposited on catalysts greatly affects the MTO reaction while its generation is very slow. It normally takes tens of minutes or even hours for catalysts to reach the desired level of coke content. Time-dependent computational fluid dynamics (CFD) simulation of such a long process poses a big challenge to reactive multiphase flow modeling. To speed up it, we try to integrate the classic chemical reaction engineering (CRE) model with CFD. In particular, the continuous stirred tank reactor (CSTR) model is established to estimate the steady state distribution of coke content, which is then set as the initial distribution for CFD simulation to shorten the time to reach the steady state of reactive flows. Comparison with experimental data shows good agreement and also great speed-up ratio compared to traditional CFD simulation.

© 2016 Elsevier Ltd. All rights reserved.

1. Introduction

The process of methanol-to-olefins (MTO) enables economical production of ethylene and propylene from coal or natural gas, and hence greatly reduces the dependence on petroleum resources. This alternative route to olefins has attracted much attention in recent years. In China, the dimethyl ether or methanol to olefins (DMTO) process (Wu and He, 2015), which was developed by the Dalian Institute of Chemical Physics (DICP), has been commercialized with a methanol feed of 1800 kt/a in Baotou, North China in August 2010 and later in many other places (Tian et al., 2015).

The development of DMTO units borrowed ideas from the reaction–regeneration design of the traditional fluid catalytic cracking (FCC) process (Tian et al., 2015). However, there is big difference between two designs. For example, a riser reactor is often used in modern FCC units to favor the endothermic catalytic cracking reaction. In contrast, a bubbling or turbulent fluidized bed reactor is preferred for exothermic methanol conversion in DMTO process. The mean residence time of catalysts in a DMTO reactor ranges from tens of minutes to hours whereas that in a FCC reactor is much shorter. Aside from the MTO reaction kinetics (to mention but a few of the related researches, e.g., Bos et al., 1995; Les-thaeghe et al., 2007; Hu et al., 2010; Kaarsholm et al., 2010,2011), the big difference between the designs of DMTO and FCC reactors leaves us much room for optimization. That requires in-depth

* Corresponding authors. Tel.: +86 10 8254 4837; fax: +86 6255 8065.

E-mail addresses: wangwei@ipe.ac.cn (W. Wang), maoye@dicp.ac.cn (M. Ye).

understanding of the coupling between hydrodynamics and reactions.

The classic chemical reaction engineering (CRE) models, e.g., plug flow reactor model and continuous stirred tank reactor (CSTR) model, have been widely applied to simplify the coupling between chemical kinetics and hydrodynamics (Levenspiel, 1999). Alwahabi and Froment (2004) applied both SAPO-based and ZSM-5-based MTO kinetics in the multi-tubular quasi-isothermal reactor model, multi-bed adiabatic reactor model and bubbling fluidized bed model, respectively, to find the optimal design for MTO reactors. Soundararajan et al. (2001) studied the MTO reactor performance based on a core-annulus two-phase model with the lumped kinetics proposed by Bos et al. (1995). Generally, CRE models are suitable for predicting time-mean, steady state behaviors of reactors.

In recent decades, computational fluid dynamics (CFD) has received rapidly growing attention as a powerful tool to explore the hydrodynamic and reactive behaviors in MTO reactors. Chang et al. (2013) extended the work of Soundararajan et al. (2001) by using a two-fluid model (TFM) in place of the core-annulus model. The three-dimensional (3D) MTO reactor (diameter: 0.2 m; height: 10 m) was operated under fast fluidization in their modeling, thus the mean residence time of catalysts was short, as in the case of FCC riser, so was the amount of coke deposited per pass. In order to maintain the desired amount of coke deposited on catalysts, they started each run with fresh catalysts and kept them participating in reactions until the desired coke content was reached, and afterwards circulated them to the regenerator (Soundararajan et al., 2001). In their work, a series of coke contents were investigated to search for the optimal value. Zhuang et al. (2014) combined the discrete element method (DEM) and CFD to simulate a small 2D MTO reactor (width: 0.16 m; height: 0.8 m). The lumped kinetic model was the same as in Chang et al. (2013). Due to the high demand of DEM simulations, they restrained their work to a limited number of 40,000 particles and gave no comparison to experimental data. Recent development of the coarse-grained DEM may pave the way for future simulation of large-scale systems (Sakai and Koshizuka, 2009). Zhao et al. (2013b) applied a two-fluid modeling with the EMMS/bubbling drag, which was proposed by Shi et al. (2011), to account for the void structure in a 16 kt/a DMTO reactor, where the catalyst were fed to the reactor from the top and discharged from the bottom, forming a counter-current turbulent flow. Their simulation results showed good agreement with hydrodynamic data of experiments in terms of void fraction and pressure distribution. The time-mean flow parameters were then incorporated into species transport equations to predict the product distribution. Such a one-way, time-mean simulation neglects the interaction between transient hydrodynamics and reactions. Thus it is not suitable for revealing the time-dependent, reactive behavior of DMTO reactors. For example, the coke is critical to methanol conversion (Hu et al., 2010; Soundararajan et al., 2001; Tian et al., 2015), whereas its concentration keeps rising in the reactor before it is burnt in the regenerator. Thus the time-dependent coking behavior is important to understand the conversion and selectivity, which suggests a transient simulation for reactive processes of MTO. However, the time step restricted by the CFL criterion is quite small for CFD simulation of a fluidized bed, normally in the order of 10^{-5} – 10^{-4} s. For such a process elapsed for even several minutes (around one tenth of the mean residence time of a real DMTO reactor), it takes several months for a mainstream computer cluster. Obviously, such a big gap between the current computing capability and industrial need poses a grand challenge to the time-

dependent CFD simulation, in particular for a reactor like DMTO, with long residence time.

In literature, it has been revealed that a reasonable initial distribution can be used to speed up hydrodynamic simulations. As discussed in Liu et al. (2011) and Zhao et al. (2013a), if one sets the initial distribution of solids with the steady-state profile of solids volume fraction predicted with the energy-minimization multi-scale (EMMS) model (Li and Kwauk, 1994), the time elapsed from initialization to reaching the steady state of flow can be greatly reduced. Likewise, for a reactive two-phase flow, we can expect a reasonable steady-state distribution of the reactants may also speed up the reactive simulation.

Bearing in mind the steady-state feature of the CRE models, we aim to combine the classic CRE and CFD approaches to realize the prediction of the long-residence-time, reactive behavior of the DMTO reactor. The Eulerian–Eulerian approach, namely TFM, is chosen for CFD simulation of fluidized bed, while the CRE model, e.g., the continuous stirred tank reactor (CSTR) model, is used to estimate the steady-state distribution of coke content, which is then set as the initial condition for the CFD simulation. Simulation results of hydrodynamics and product distribution are presented with comparison to experimental data. Finally, we discuss the future work for elaborating the current method to speed up the two-phase reactive flows.

2. Model and settings

2.1. DMTO reactor

The pilot-scale DMTO reactor with a methanol feed of 100 t/a is shown in Fig. 1. The main reaction zone is a bubbling reactor with 0.261 m I.D. and height of 1.347 m. The main stream of reactants, methanol (MeOH) and steam (H_2O) flows into the bubbling reactor from below the distributor with a total flow rate of 27 kg/h (the mass ratio of MeOH to H_2O is 2:1). Another stream of steam enters the lifting tube through a horizontal pipe with a flow rate of 0.12 kg/h. Fresh catalysts are fed into the sedimentation bed with a flow rate of 8.8 kg/h. The MTO reactions occur once the methanol

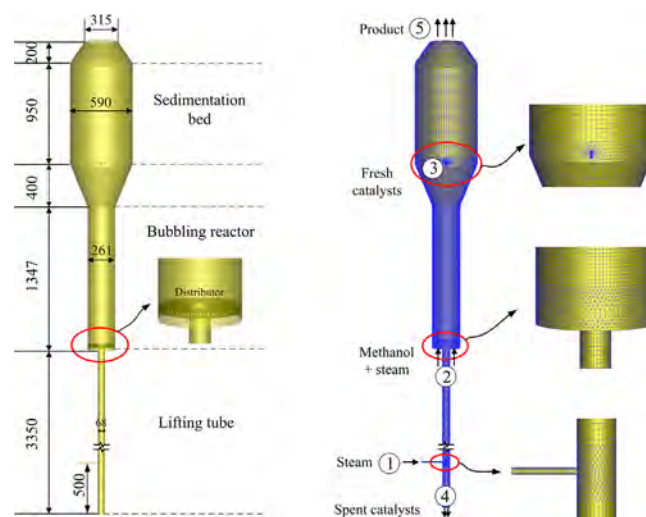


Fig. 1. The geometry of the DMTO reactor (LHS) and its mesh and boundary conditions (RHS). (1) steam (mass flow inlet); (2) methanol–steam mixture (mass flow inlet); (3) catalyst inlet (velocity inlet); (4) catalyst outlet (velocity inlet); and (5) gaseous product (pressure outlet).

interacts with catalysts with a heat release of 22.5 kJ/mol. The produced coke is deposited on catalysts and in turn affects the reaction rates. Spent catalysts are finally discharged through the central opening of the distributor to the bottom of the lifting tube and then transported to the regenerator. The gaseous products are released from the top exit. The more details of the operating conditions are listed in Table 1.

2.2. Governing equations and constitutive relations

The Eulerian multiphase granular model in ANSYS Fluent version 15 is employed. The governing equations and constitutive relations are summarized in Table 2 (ANSYS Inc., 2013). The species and energy transport equations are turned on to take into account the chemical reactions. The kinetic theory for granular flow (Gidaspow, 1994) is applied to close the solids stress. It is recognized that the drag coefficient is greatly affected by inhomogeneous flow structures (Li et al., 1993; O'Brien and Syamlal, 1993; Agrawal et al., 2001; Yang et al., 2003; Wang and Li, 2007; Lu et al., 2009; Hong et al., 2012; Wang et al., 2012). In this work, the EMMS/bubbling drag model, which was proposed by Shi et al. (2011) and further developed by Hong et al. (2013), is chosen, since the DMTO reactor is operated in the bubbling fluidization regime

at the lab and pilot scales and turbulent fluidization regime at the demo and commercial scales (Tian et al., 2015). This drag model, in which bubbles are considered as the meso-scale structures, has been applied in previous DMTO simulations (Zhao et al., 2013b) and now has become a module in the software EMMS[®]2.0. Under the operating conditions for the DMTO reactor, the drag correction curve, which is measured with the heterogeneity index, H_D , is shown in Fig. 2. H_D converges to unity at the two ends of the abscissa, and its minimum value appears at the voidage of about 0.5. The fitting functions for H_D are summarized in Table 2. For the voidage out of the range ($\epsilon_{mf}, 1$), H_D is set to be unity.

2.3. DMTO reaction kinetics

The lumped reaction kinetics for DMTO, as shown in Fig. 3, consists of a set of parallel reactions, where MeOH refers to methanol, DME refers to dimethyl ether and C₄ and C₅ are represented by C₄H₈ and C₅H₁₀.

Table 1
Operating conditions.

Lifting steam inflow rate, kg/h	0.12
Main inflow rate of methanol and steam, kg/h	27
Mass ratio of MeOH:H ₂ O in main stream	2:1
Fresh catalyst inflow rate, kg/h	8.8
Fresh catalyst inlet area, m ²	0.000144
Spent catalyst outflow rate, kg/h	8.8
Spent catalyst outlet area, m ²	0.0036
Gauge pressure at top exit, MPa	0.024
Catalyst inventory in bubbling reactor, kg	9
Solid volume fraction in lifting tube	0.6
Temperature in bubbling bed, T _b , K	738

Table 2
Governing equations and constitutive relations.

Continuity equation ($q=g, s$)	(A)	Granular temperature equation	(I)
$\frac{\partial}{\partial t}(\epsilon_q \rho_q) + \nabla \cdot (\epsilon_q \rho_q \mathbf{u}_q) = 0$		$\frac{3}{2} \left[\frac{\partial}{\partial t}(\epsilon_s \rho_s \Theta_s) + \nabla \cdot (\epsilon_s \rho_s \mathbf{u}_s \Theta_s) \right] = \tau_s : \nabla \mathbf{u}_s - \nabla \cdot \mathbf{q} - \gamma - 3\Theta_s \beta$	
Momentum equations of gas and solid phases	(B)	Collisional energy dissipation	(J)
$\frac{\partial}{\partial t}(\epsilon_g \rho_g \mathbf{u}_g) + \nabla \cdot (\epsilon_g \rho_g \mathbf{u}_g \mathbf{u}_g)$ $= -\epsilon_g \nabla p + \nabla \cdot \tau_g + \epsilon_g \rho_g \mathbf{g} + (\mathbf{u}_s - \mathbf{u}_g) \beta$		$\gamma = (1 - e^2) \epsilon_s^2 \rho_s g_0 \frac{12}{d_s} \Theta_s^3 / 2$	
$\frac{\partial}{\partial t}(\epsilon_s \rho_s \mathbf{u}_s) + \nabla \cdot (\epsilon_s \rho_s \mathbf{u}_s \mathbf{u}_s)$ $= -\epsilon_s \nabla p - \nabla p_s + \nabla \cdot \tau_s + \epsilon_s \rho_s \mathbf{g} + (\mathbf{u}_g - \mathbf{u}_s) \beta$		Solid phase shear viscosity	(K)
Species equation ($q=g, s$)	(C)	$\mu_s = \mu_{s,col} + \mu_{s,kin} + \mu_{s,fr}$	
$\frac{\partial}{\partial t}(\rho_q \epsilon_q Y_{q,i}) + \nabla \cdot (\rho_q \epsilon_q \mathbf{u}_q Y_{q,i})$ $= -\nabla \cdot \epsilon_q \mathbf{J}_{q,i} + \epsilon_q R_{q,i}$		$\mu_{s,col} = \frac{4}{3} \epsilon_s \rho_s d_s g_0 (1 + e) \sqrt{\frac{\Theta_s}{\pi}}$	(L)
Stress tensors for gas and solid phases	(D)	$\mu_{s,kin} = \frac{10 \rho_s d_s \sqrt{\Theta_s \pi}}{96 \epsilon_s (1 + e) g_0} \left[1 + \frac{4}{3} (1 + e) \epsilon_s g_0 \right]^2$	(M)
$\tau_g = \epsilon_g \mu_g \left[\nabla \mathbf{u}_g + (\nabla \mathbf{u}_g)^T \right] - \frac{2}{3} \epsilon_g \mu_g \nabla \cdot \mathbf{u}_g$		$\mu_{s,fr} = \frac{\rho_s \sin \varphi}{2 \sqrt{1 + 2\varphi}}$	(N)
$\tau_s = \epsilon_s \mu_s \left[\nabla \mathbf{u}_s + (\nabla \mathbf{u}_s)^T \right] + \epsilon_s (\lambda_s - \frac{2}{3} \mu_s) \nabla \cdot \mathbf{u}_s$	(E)	Gas-solid drag coefficient	(O)
Solid phase pressure	(F)	$\beta = \frac{3}{4} C_D \frac{\rho_g (1 - \epsilon_g) \epsilon_g}{d_s} \mathbf{u}_g - \mathbf{u}_s \epsilon_g^{-2.65} H_D$	
$p_s = \epsilon_s \rho_s \Theta_s [1 + 2(1 + e) \epsilon_s g_0]$		$H_D = 0.1443 + \frac{1.6864}{1 + (\epsilon_g / 0.4064)^{20.4805}}$, $\epsilon_g \in (\epsilon_{mf}, 0.4924)$	
Solid phase bulk viscosity	(G)	$H_D = (-0.0999 + 0.9586 \epsilon_g)^{1.8008}$, $\epsilon_g \in (0.4924, 0.9505)$	
$\lambda_s = \frac{4}{3} \epsilon_s \rho_s d_s g_0 (1 + e) \sqrt{\frac{\Theta_s}{\pi}}$		$H_D = (1649.4591 - 1648.5453 \epsilon_g)^{0.08597}$, $\epsilon_g \in (0.9505, 1)$	
Radial distribution function	(H)		
$g_0 = \left[1 - \left(\frac{\epsilon_s}{\epsilon_{sm}} \right) \right]^{-2.5 \epsilon_{sm}}$			

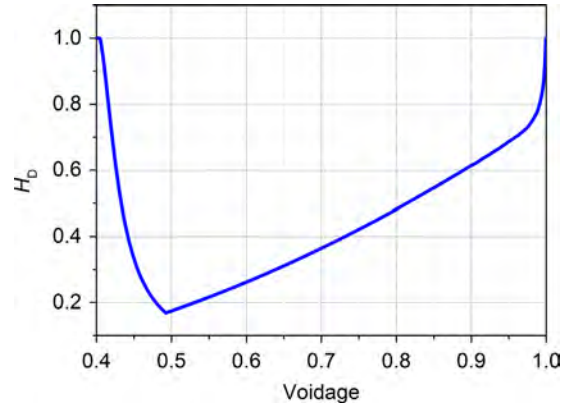


Fig. 2. The heterogeneity index, H_D , of EMMS/bubbling drag by using EMMS[®]2.0 ($\rho_g = 0.4288 \text{ kg/m}^3$, $\mu_g = 2.43 \times 10^{-5} \text{ Pa s}$, $d_s = 97 \text{ }\mu\text{m}$, $\rho_s = 1500 \text{ kg/m}^3$, $u_0 = 0.327 \text{ m/s}$, $\epsilon_{mf} = 0.4$).

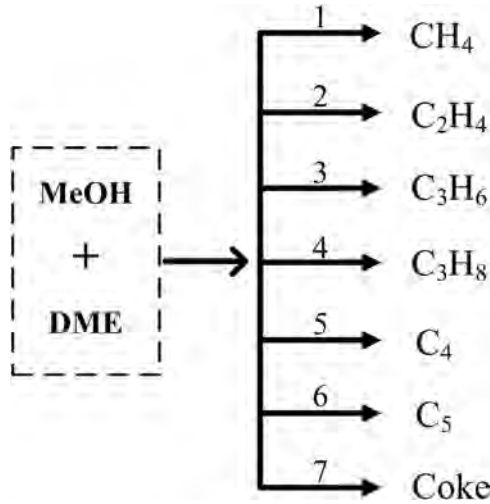


Fig. 3. The route of DMTO reactions.

Table 3
MTO reaction rate constant k_i and a_i .

Reaction no.	Rate constant k_i (L/g _{cat} /s)			Parameter a_i		
	723 K	748 K	763 K	723 K	748 K	763 K
1	0.00232	0.00300	0.00501	0.0576	0.0649	0.043
2	0.10030	0.12463	0.15413	0.0914	0.1008	0.0982
3	0.15817	0.16212	0.19234	0.1743	0.1996	0.2017
4	0.03699	0.03467	0.04252	0.3462	0.406	0.4099
5	0.07519	0.07910	0.09094	0.2575	0.2924	0.2929
6	0.05159	0.04895	0.04895	0.3759	0.3495	0.3336
7	0.05436	0.05859	0.07432	0.3817	0.3856	0.3793

The formation rate of each lump, R_i ($i = \text{CH}_4, \text{C}_2\text{H}_4, \text{C}_3\text{H}_6, \text{C}_3\text{H}_8, \text{C}_4\text{H}_8, \text{C}_5\text{H}_{10}, \text{MeOH}$ and H_2O) is:

$$R_{\text{CH}_4} = k_1 \varphi_1 C_{\text{MeOH}} M_{\text{CH}_4}, \quad (1)$$

$$R_{\text{C}_2\text{H}_4} = \frac{1}{2} k_2 \varphi_2 C_{\text{MeOH}} M_{\text{C}_2\text{H}_4}, \quad (2)$$

$$R_{\text{C}_3\text{H}_6} = \frac{1}{3} k_3 \varphi_3 C_{\text{MeOH}} M_{\text{C}_3\text{H}_6}, \quad (3)$$

$$R_{\text{C}_3\text{H}_8} = \frac{1}{3} k_4 \varphi_4 C_{\text{MeOH}} M_{\text{C}_3\text{H}_8}, \quad (4)$$

$$R_{\text{C}_4} = \frac{1}{4} k_5 \varphi_5 C_{\text{MeOH}} M_{\text{C}_4}, \quad (5)$$

$$R_{\text{C}_5} = \frac{1}{5} k_6 \varphi_6 C_{\text{MeOH}} M_{\text{C}_5}, \quad (6)$$

$$R_{\text{Coke}} = \frac{1}{6} k_7 \varphi_7 C_{\text{MeOH}} M_{\text{Coke}}. \quad (7)$$

The total reaction rate for methanol and water has the following expressions:

$$R_{\text{MeOH}} = - \left(\sum_1^6 k_i \varphi_i \right) C_{\text{MeOH}} M_{\text{MeOH}}. \quad (8)$$

$$R_{\text{H}_2\text{O}} = \left(\sum_1^6 k_i \varphi_i \right) C_{\text{MeOH}} M_{\text{H}_2\text{O}}, \quad (9)$$

where C_{MeOH} denotes the methanol concentration, (mol/L); M denotes the molar weight, g/mol; k_i is the reaction rate constant corresponding to lump i , (L/g_{cat}/s) and φ_i is the deactivation function, defined by

$$\varphi_i = \frac{A}{1 + B \exp(D \times (w_c - E))} \exp(-\alpha_i w_c), \quad (10)$$

where $A=1$, $B=9$, $D=2$, and $E=7.8$. w_c is the coke content, (g/100g_{cat}). The C_6+ components lead to deactivation of catalyst and can be viewed as coke (its molar weight is 84 g/mol) because they cannot escape from the SAPO-34 cages. The rate constant k_i and a_i at different temperatures are listed in Table 3.

2.4. Simulation settings

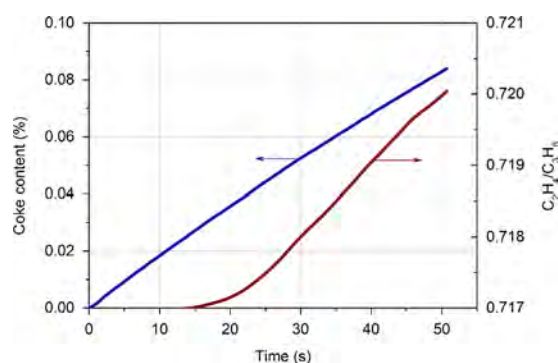
The mesh and boundary settings for this pilot-scale DMTO reactor are also shown in Fig. 1. Hexahedral cells are generated by using Gambit[®] 2.4 for most of computation zones, except for the regions near the distributor and the steam and catalyst inlets, where tetrahedral cells are employed. All the computational cells total about 350,000, in which nearly 210,000 cells are generated for meshing the bubbling reactor and 63,000 cells for meshing the region near the distributor (averaged cell size is about 70 times particle diameter), since most reactions take place near the distributor according to Zhao et al. (2013b). Such resolution is acceptable since our previous work (Lu et al., 2009, 2013; Zhang et al., 2010) indicated that the coarse-grid simulation of fluidized bed with the EMMS drag allows reasonable prediction if the cell size is within the range of 10–100 times the particle diameter. The original design of the distributor combines sieve and sintered plate. Here it is simplified to a perforated plate with opening ratio of 5%.

The mass flow inlet is prescribed for both the steam inlet (1) and methanol–steam mixture inlet (2). The velocity inlet is specified for the catalyst inlet (3) and the bottom catalyst outlet (4). To keep a constant solids inventory in the bed, the mass flow rates at inlets (3) and (4) add up to zero. The solids volume fraction for catalyst inlet (3) is set to be 0.4 and coke content 2%. The solids volume fraction and the coke content at the catalyst outlet (4) are set equal to those in the neighboring cells. The top product outlet (5) is prescribed with a gauge pressure of 0.024 MPa. The no-slip wall boundary is set for both the gas and solid phases.

Both gas and solid phases are treated as mixtures in simulation. There are nine species in the gas mixture, i.e., CO_2 , CH_4 , C_2H_4 , C_3H_6 , C_3H_8 , C_4H_8 , C_5H_{10} , H_2O and MeOH . In particular, CO_2 is introduced intentionally as an “inert” gas and the last species so as not to react with the other chemical substances. All the other eight species are produced or consumed in the course of reactions and their mass changes are expressed in forms of source terms on the right hand side of the species transport equations in Table 2. The molecular weight of each gas species is obtained from NIST database (<http://webbook.nist.gov/chemistry/>). The heat capacity and thermal conductivity for gas species are obtained from Aspen Plus[®] 7.2. The viscosities are taken from Tong and Li (1982). The solid phase has two species, coke and catalyst, on which the same heat capacity (1220 J/(kg K)) and thermal conductivity (0.0454 W/(m K)) are assumed. The catalyst diameter and density are 97 μm and 1500 kg/m³, respectively. The densities for gas and solid mixtures are calculated with the incompressible ideal gas equation and the volume-weighted mixing law, respectively. The other properties for both mixtures are based on the mass-weighted mixing law. To ensure better convergence, the algebraic form of the granular

Table 4
Simulation settings.

Pressure-velocity coupling	Phase coupled SIMPLE
Discretization for momentum	Second order upwind
Discretization for volume fraction	Quick
Discretization for each species	First order upwind
Transient formulation	First order upwind
Granular viscosity	Gidaspow (Eq. (K) in Table 2)
Granular bulk viscosity	Lun-et-al (Eq. (G) in Table 2)
Frictional viscosity	Schaeffer (Eq. (N) in Table 2)
Angle of internal friction	30.00007
Frictional pressure	Based-ktgf
Frictional modulus	derived
Friction packing limit	0.61
Granular temperature	Algebraic form of Eq. (I) in Table 2
Solids pressure	Lun-et-al (Eq. (F) in Table 2)
Radial distribution	Lun-et-al (Eq. (H) in Table 2)
Elasticity modulus	derived
Packing limit	0.63
Drag model	EMMS/bubbling (Eq. (O) in Table 2)
Time step	0.0005 s

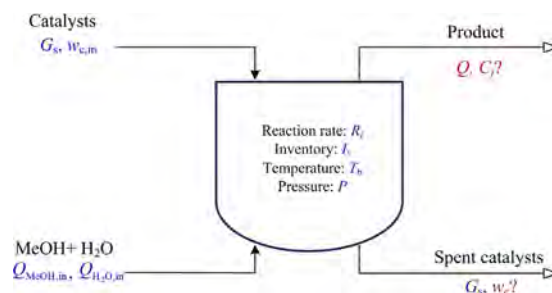
**Fig. 4.** The time-dependent variation of the mass-weighted-average coke content and the ratio of C_2H_4 to C_3H_6 in the bubbling reactor.

temperature model is chosen in our simulations. Such an approximation is also helpful to save run time and allows reasonable agreement with experiments of bubbling fluidized bed (Bakshi et al., 2014). Detailed settings are referred to Table 4.

3. CRE-estimated initial distribution

As shown in Eqs. (1)–(9), coke content greatly affects the reaction rate. Fig. 4 shows the increase of coke content with time in the bubbling reactor at temperature of 738 K. The generation rate of coke is rather low. After an elapse of 50 s, the coke content amounts to about 0.08%. The ratio of C_2H_4 to C_3H_6 increases with coke content during this period of time, but it is still far less than the measurement (1.24) by the end of 50 s. Indeed in real practice, it requires a run for about one hour to reach the desired level of coke content (empirically 6%) if the reactor starts with fresh catalysts without coke deposited. And that is estimated to take 1200 days on our parallel computers (2CPUs per node, Intel-Xeon 2.8G, 10 cores). Obviously, such a speed is too low and not affordable to most of available computer resources.

Because the coke production rate is low and the solid catalysts are well mixed, as a first approximation, here we use the CSTR model to estimate the coke concentration in the bubbling fluidized

**Fig. 5.** The CSTR model for the DMTO reactor (the blue ones are inputs and red ones are to be determined). (For interpretation of the references to color in this figure legend, the reader is referred to the web version of this article.)**Table 5**

Mass fractions of gaseous products and other quantities predicted by using CSTR (the mass fractions are recalculated by removing H_2O , methanol and CO_2).

	CSTR	Exp.	Error (%)
Y_{CH_4}	0.01468	0.01643	10.651
$Y_{C_2H_4}$	0.4432	0.4303	2.986
$Y_{C_3H_6}$	0.3673	0.3457	6.257
$Y_{C_3H_8}$	0.02874	0.03788	24.129
Y_{C_4}	0.1073	0.0913	17.536
Y_{C_5}	0.03877	0.07836	50.523
w_c (%)	5.6498	~6	~5.837
η_{MeOH} (%)	98.3126	99.9444	1.633
$S_{C_2H_4+C_3H_6}$	81.05	77.603	4.442
C_2H_4/C_3H_6	1.2066	1.2449	3.0766

bed. As shown in Fig. 5, all the symbols in blue are model inputs and the others in red are the variables to be determined. The associated conservation relations of species are given in Eqs.(11)–(13):

Balance of coke

$$G_s w_{c,in} + I_s R_c = G_s w_c, \quad (11)$$

Balance of reactants and gaseous products

$$Q_{j,in} C_{j,in} + I_s R_j / M w_j = Q C_j, \quad (12)$$

Pressure balance at exit

$$\sum_{j=CH_4}^{MeOH} C_j = \frac{P}{1000RT_b}, \quad (13)$$

where G_s (g/s) represents the mass flow rates of catalysts through the system, I_s total catalyst inventory (g) and Q (L/s) the volumetric flow rate of gas phase, respectively. The subscript j represents all the gaseous species. The constant pressure and temperature are assumed in this CSTR model. In the CSTR model, all the species concentrations at the exit are the same as those in the reactor.

Table 5 shows the model solutions. Generally the predicted mass fraction (Y) of gaseous products, coke content (w_c), selectivity of C_2H_4 and C_3H_6 ($S_{C_2H_4+C_3H_6}$) and ratio of C_2H_4 to C_3H_6 agree with the experimental data at the specified bed temperature of 738 K. The methanol conversion, η_{MeOH} , is relatively under-predicted. Such a discrepancy is understandable since the impacts of dynamic flow structure and the pressure change are not considered in the CSTR model. The mean coke concentration determined in this approach is then set as the initial condition for the following CFD simulation.

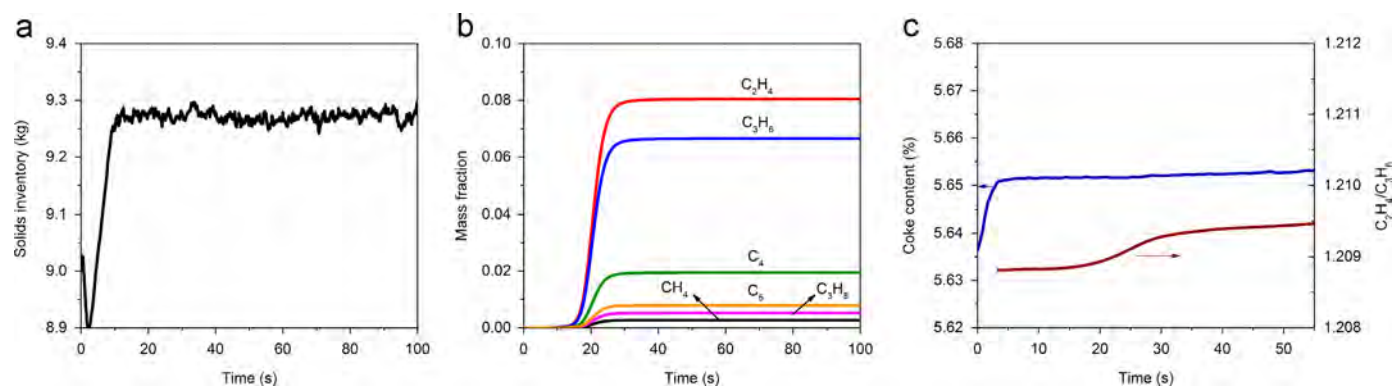


Fig. 6. Evolution of solids inventory, mass fraction of each gaseous product, coke content as well as C_2H_4/C_3H_6 : (a) volume-weighted-average solids inventory in the bubbling reactor; (b) mass fraction of each gaseous product at the top outlet; and (c) mass-weighted-average coke content in the bubbling reactor as well as C_2H_4/C_3H_6 .

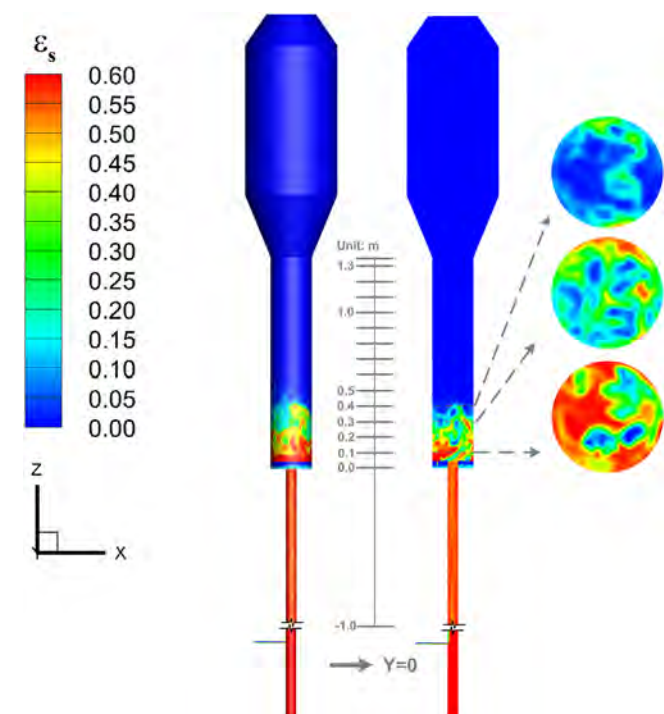


Fig. 7. The instantaneous distribution of solids volume fraction over the whole bed and on the planes of $Y=0$ and $Z=0.1$ m, 0.3 m and 0.4 m.

4. CFD simulation results

Given the initial distribution of coke, once the simulation starts, the total solids inventory in the DMT reactor keeps constant as the solids mass flow out is set equal to the solid mass flow in. However, the solids are re-allocated in different sections of the bed. Fig. 6 displays the evolution of solids inventory, the mass fractions of gaseous products, coke content as well as C_2H_4/C_3H_6 . The solids inventory in the bubbling reactor quickly reaches its steady-state value after an elapse of around 10 s (Fig. 6a). The gaseous products can be detected after 10 s at the top outlet, and their contents quickly converge to the steady-state values, reaching an equilibrium after about 40 s, as shown in Fig. 6b. The coke content changes rapidly at the initial period, and then levels off (Fig. 6c). The ratio of C_2H_4 to C_3H_6 increases with coke content,

then gradually approaches the steady state value of 1.21, very close to the measurement (1.24). Time-averaged statistics start after 60 s and elapse for over 40 s. One simulation case takes about 30 days.

4.1. Hydrodynamic distributions

Fig. 7 shows instantaneous distribution of solids volume fraction across the whole bed. A typical bubbling fluidization state is captured in the bubbling reactor section, with bed surface at the elevation of around 0.4 m. The axial and radial profiles of time-mean solids volume fraction are shown in Fig. 8. Below 0.4 m, all the cross-sectionally time-mean solids volume fraction are greater than 0.1. And the radial profiles at the elevations of 0.1 m, 0.3 m and 0.4 m show the highest solids volume fraction near the wall, but their lowest values deviate from the center, indicating obvious asymmetries. That may be caused by the combined effects of the upper feeding and the lifting steam flow from the bottom.

Fig. 9 gives the close-up of the velocity vector of the solid phase at the bottom of the bubbling reactor. Particles move down along the wall and averts their movement from upflowing gas, thus forming vortices. At the interface between the bubbling reactor and the lifting tube, the catalyst drops due to reduced gas velocity.

4.2. Distribution of coke content

Fig. 10 shows instantaneous distribution of coke content at no. 60 s, 80 s and 100 s, respectively, together with the axial profile of time-mean, cross-sectionally averaged coke content. At all these instants, the coke content appears to be quite uniform below 0.5 m, indicating strong back mixing in this region. That also partly explains why we can use the CSTR model to estimate the coke content. Above 0.5 m, the radial profiles become uneven and the coke content generally decreases along the height and almost vanishes at the elevation of about 2.0 m. The mean coke content in the entire range of the bubbling reactor shown in the red square of the right graph, changes between about 4.5% and 5.65%.

4.3. Distribution of gaseous products

Ethylene and propylene are two main gaseous products of MTO. Fig. 11 shows the contour of mass fraction of C_2H_4 and C_3H_6 on the plane of $Y=0$ and three cross sections. Similar distribution is observed for C_2H_4 and C_3H_6 except the difference in magnitude. That is because the reactions producing C_2H_4 and C_3H_6 are parallel and the mass diffusivity is set as the same for all species in the gas

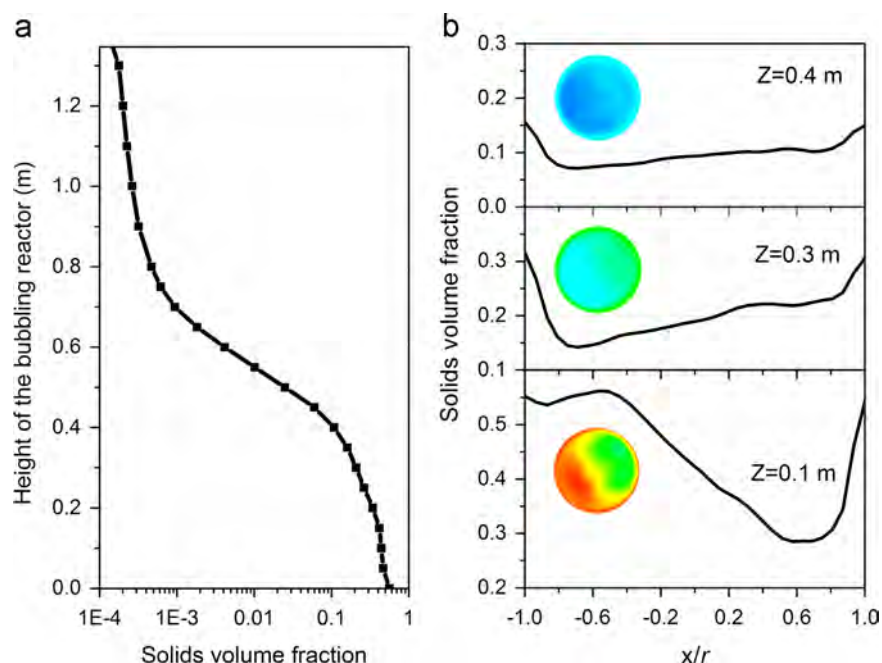


Fig. 8. Axial and radial profiles of time-mean solids volume fraction in the bubbling reactor: (a) the axial profile; and (b) the radial profiles on the planes of $Z=0.1$ m, 0.3 m and 0.5 m.

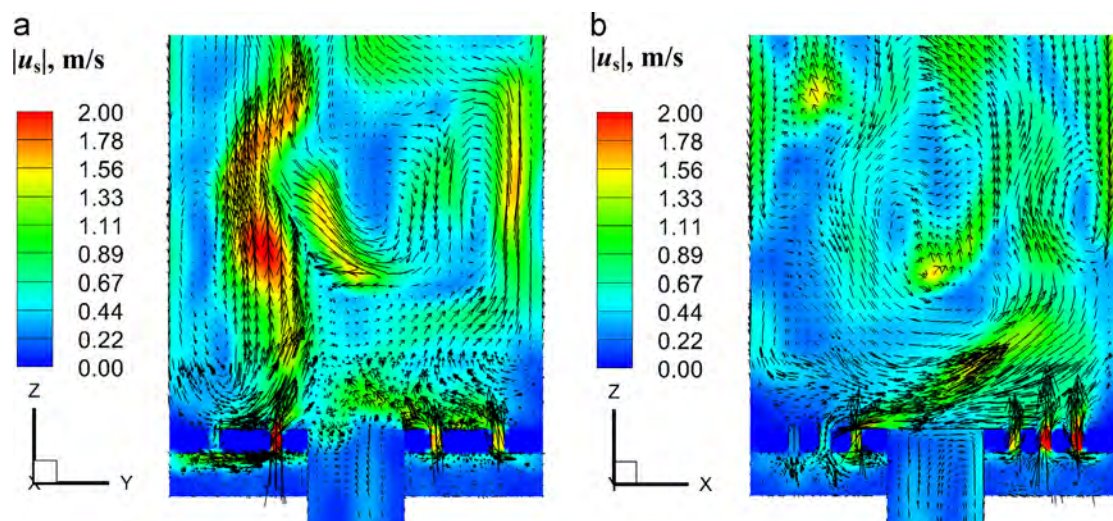


Fig. 9. A close-up of the transient velocity vector of solid phase at the bottom of the bubbling reactor: (a) plane of $X=0$; and (b) plane of $Y=0$.

mixture. The reactions seem to be almost completed near the distributor below the elevation of 0.2 m, above which the concentration distributions in both axial and radial directions appear to be uniform. Fig. 12 gives quantitative curves of the mass fractions of C_2H_4 and C_3H_6 . The radial distributions of the gaseous products seem to be influenced greatly by the distributor. Near the distributor ($Z=0.047$ m), the “W-shape” profiles are captured and above 0.2 m, the influence of the distributor become less important and then flat curves are observed at the top of Fig. 12b.

Table 6 shows the mass fraction of gaseous products, coke content, methanol conversion, selectivity of light olefins (C_2H_4 and C_3H_6) and the ratio of C_2H_4 to C_3H_6 predicted by our CFD simulation, together with its comparison to experimental data. Compared to Table 5, most CFD results are close to CSTR predictions, and only the methanol conversion predicted by CFD simulation is much closer to experimental data than the CSTR one. That may be

attributed to the more realistic, dynamic simulation of CFD. The same findings are also observed in the other cases under different operating conditions, which are not detailed here. In our future work, the heat transfer between walls and the inner flow will be taken into account since the temperature gradient should be more important, especially near the wall and distributor in large-scale MTO or MTP reactors.

5. Conclusions and future work

In this study, a 3D transient iso-thermal simulation based on combination of two-fluid model and chemical kinetics are carried out to explore the hydrodynamic and reactive behavior of a pilot-scale DMTO reactor. The EMMS/bubbling model is chosen to calculate the drag force between the gas and solid phases.

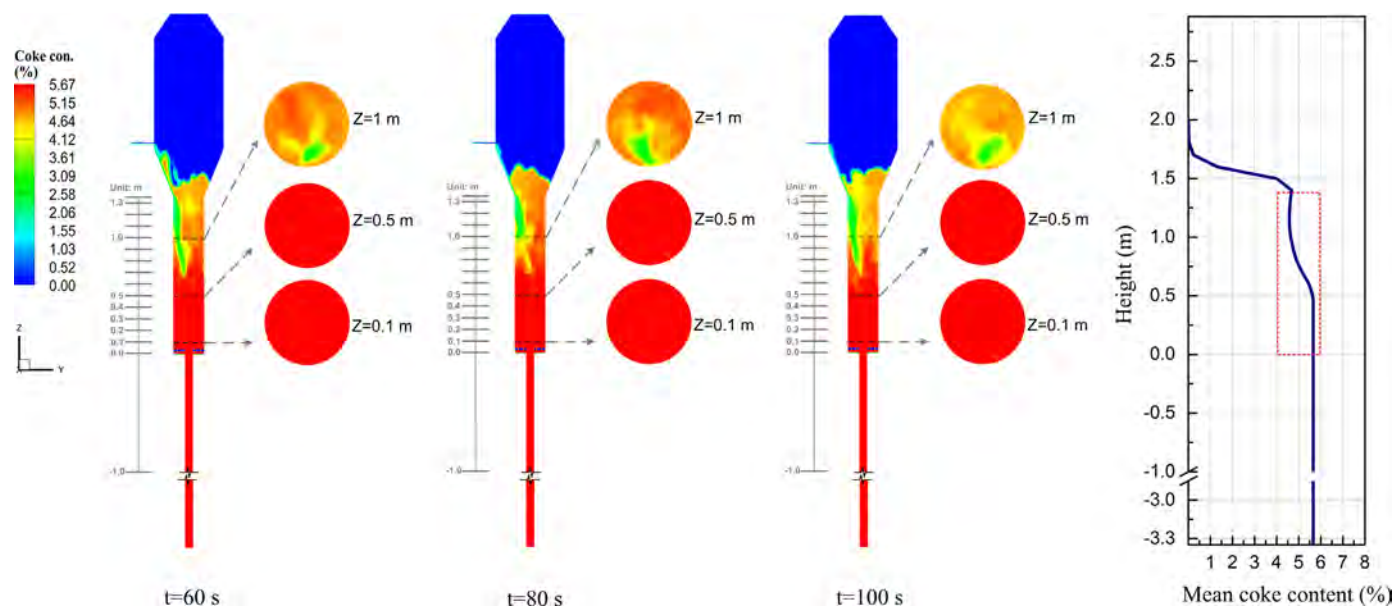


Fig. 10. Snapshots of coke content on the planes of $X=0$ and elevations of $Z=0.1$ m, 0.5 m and 1 m at no. 60 s, 80 s and 100 s, respectively, together with the axial profile of the mean coke content.

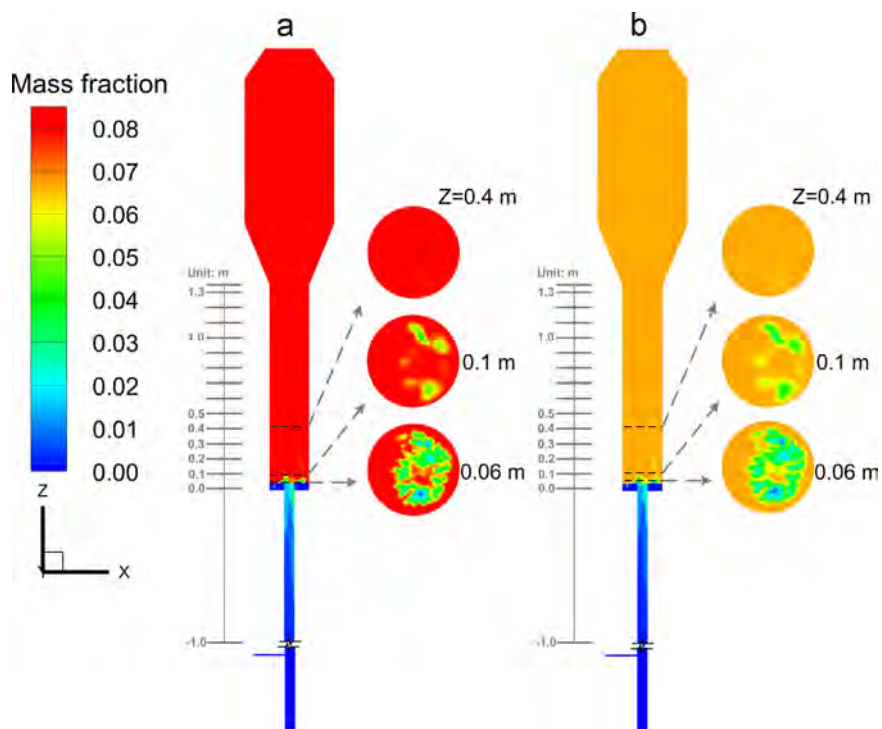


Fig. 11. The instantaneous distributions of mass fraction of C_2H_4 and C_3H_6 on the planes of $Y=0$ and $Z=0.06$, 0.1 , and 0.4 m: (a) C_2H_4 ; (b) C_3H_6 .

Considering the long-residence-time characteristics of the DMTO process, we establish a CSTR model to estimate the coke concentration for initialization of CFD, thus greatly shortening the transition time from the initial state to the steady state. The typical behaviors of the bubbling fluidized bed and countercurrent flow are captured in our simulations. Great change of mass fractions of C_2H_4 and C_3H_6 is found in the region near the distributor. That reminds us that more simulation efforts are needed in this region. The iso-thermal CFD simulation predicts similar product concentrations as in the CSTR model except better prediction of

methanol conversion. Generally the combination of CFD and CRE brings us better capability for reactive simulation of fluidized beds with long residence time.

In future work, the EMMS/bubbling drag should be modified to cope with the regime change from the bubbling to turbulent fluidization. Additionally, the non-isothermal operation requires more realistic coupling among hydrodynamics and heat transfer as well as reactions. A reasonable initial distribution of temperature might also be required that deserves more elaborate CRE modeling of reactors.

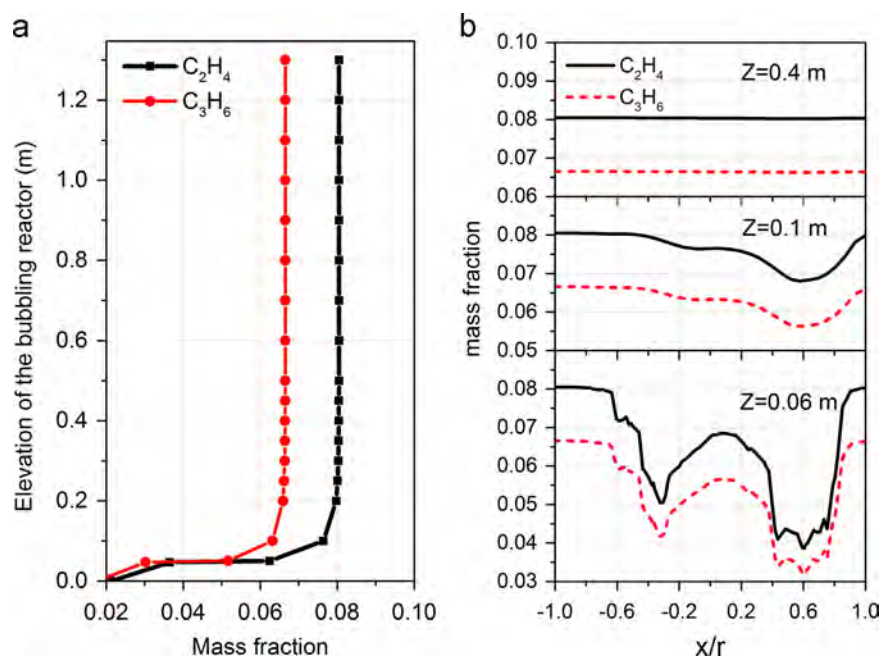


Fig. 12. The axial and radial profiles of time-mean mass fraction of C_2H_4 and C_3H_6 in the bubbling reactor: (a) axial profiles; (b) radial profiles on the planes of $Z=0.06$ m, 0.1 m and 0.4 m.

Table 6

Comparison of mass fraction of gaseous products and other quantities obtained by CFD simulation and experiments (the mass fractions are recalculated by removing H_2O , methanol and CO_2).

	Simulation	Exp.	Error (%)
Y_{CH_4}	0.01466	0.01643	10.773
$Y_{C_2H_4}$	0.4417	0.4303	2.642
$Y_{C_3H_6}$	0.3652	0.3457	5.635
$Y_{C_3H_8}$	0.02851	0.03788	24.762
Y_{C_4}	0.1066	0.0913	16.736
Y_{C_5}	0.04338	0.07836	44.640
w_c (%)	5.655	~6	~5.75
η_{MeOH} (%)	99.97	99.9444	0.0256
$S_{(C_2H_4+C_3H_6)}$	80.687	77.603	3.974
C_2H_4/C_3H_6	1.2096	1.2449	2.836

Nomenclature

C	concentration, mol/L
w_c	coke content, g/100g _{cat}
C_D	effective drag coefficient for a particle
C_{D0}	standard drag coefficient for a particle
d_{cl}	cluster diameter, m
d_s	particle diameter, m
e	restitution coefficient
G_s	Mass flow rate, g/s
g	gravitational acceleration, m/s ²
g_0	radial distribution function
H_D	heterogeneity index ($H_D = \beta/\beta_0$)
I_s	solids inventory, g
k_i	rate constant, L/(g _{cat} s)
M	molar weight, g/mol
p	pressure, Pa
Q	volumetric flow rate, L/s
q	flux of fluctuating energy, kg/s ³
r	the radius of the cross section of the bubbling bed, m
R	gas constant, 8.314, J/mol/k
R_i	reaction rate, g/(g _{cat} s)
S	selectivity (the reacted/the fed), %
T_b	temperature in the bubbling reactor, K

u	real velocity, m/s
u_0	superficial velocity, m/s
w_c	coke content, g/100g _{cat}
η	conversion (%)
Y	mass fraction

Greek letters

β	drag coefficient with structure in a control volume, kg/(m ³ s)
β_0	drag coefficient without structure in a control volume, kg/(m ³ s)
ϵ_g	voidage
ϵ_{mf}	incipient voidage (0.4)
ϵ_s	solids volume fraction
μ	viscosity, Pa s
ρ	density, kg/m ³
τ	stress tensor, Pa
Θ	granular temperature, m ² /s ²
φ	the deactivation function

Subscripts

g	gas phase
s	solid phase
i	each lump in MTO lumped reaction kinetics
j	gaseous species (bold characters are for vectors or tensors)

Acknowledgment

This work is financially supported by the National Natural Science Foundation of China under Grant nos. 21106157, 91334204 and 91334205 and the "Strategic Priority Research Program" of Chinese Academy of Sciences under Grant no. XDA07080202, and

the Ministry of Science and Technology of the People's Republic of China under Grant no. 2012CB215003.

Appendix A. Supplementary material

Supplementary data associated with this article can be found in the online version at <http://dx.doi.org/10.1016/j.ces.2016.01.010>.

References

- Agrawal, K., Loezos, P.N., Syamlal, M., Sundaresan, S., 2001. The role of mesoscale structures in rapid gas-solid flows. *J. Fluid Mech.* 445, 151–185.
- Alwahabi, S.M., Froment, G.F., 2004. Conceptual reactor design for the methanol-to-olefins process on SAPO-34. *Ind. Eng. Chem. Res.* 43, 5112–5122.
- ANSYS, Inc., 2013. ANSYS Fluent Theory Guide (release 15.0), (<http://www.ansys.com>).
- Bakshi, A., Altantzis, C., Ghoniem, A., 2014. Towards accurate three-dimensional simulation of dense multi-phase flows using cylindrical coordinates. *Powder Technol.* 264, 242–255.
- Bos, A.N.R., Tromp, P.J.J., Akse, H.N., 1995. Conversion of methanol to lower olefins. Kinetic modeling, reactor simulation, and selection. *Ind. Eng. Chem. Res.* 34, 3808–3816.
- Chang, J., Zhang, K., Chen, H., Yang, Y., Zhang, L., 2013. CFD modelling of the hydrodynamics and kinetic reactions in a fluidised-bed MTO reactor. *Chem. Eng. Res. Des.* 91, 2355–2368.
- Gidaspo D., 1994. *Multiphase Flow and Fluidization: Continuum and Kinetic Theory Descriptions*. Academic Press, Boston.
- Hong, K., Wang, W., Zhou, Q., Wang, J., Li, J., 2012. An EMMS-based multi-fluid model (EFM) for heterogeneous gas-solid riser flows: part I. Formulation of structure-dependent conservation equations. *Chem. Eng. Sci.* 75, 376–389.
- Hong, K., Shi, Z., Wang, W., Li, J., 2013. A structure-dependent multi-fluid model (SFM) for heterogeneous gas-solid flow. *Chem. Eng. Sci.* 99, 191–202.
- Hu, H., Cao, F., Ying, W., Sun, Q., Fang, D., 2010. Study of coke behaviour of catalyst during methanol-to-olefins process based on a special TGA reactor. *Chem. Eng. J.* 160, 770–778.
- Kaarsholm, M., Joensen, F., Cenni, R., Chaouki, J., Patience, G.S., 2011. MeOH to DME in bubbling fluidized bed: Experimental and modelling. *Can. J. Chem. Eng.* 89, 274–283.
- Kaarsholm, M., Rafii, B., Joensen, F., Cenni, R., Chaouki, J., Patience, G.S., 2010. Kinetic modeling of methanol-to-olefin reaction over ZSM-5 in fluid bed. *Ind. Eng. Chem. Res.* 49, 29–38.
- Lesthaeghe, D., Van Speybroeck, V., Marin, G.B., Waroquier, M., 2007. The rise and fall of direct mechanisms in methanol-to-olefin catalysis: An overview of theoretical contributions. *Ind. Eng. Chem. Res.* 46, 8832–8838.
- Levenspiel, O., 1999. *Chemical Reaction Engineering*, third ed.. John Wiley & Sons, New York.
- Li, J., Chen, A., Yan, Z., Xu, G., Zhang, X., 1993. Particle-fluid contacting in circulating fluidized beds. In: Avidan, A. A. (Ed.), Preprint Volume for CFB-IV, New York, pp. 49–54.
- Li, J., Kwauk, M., 1994. *Particle-Fluid Two-Phase Flow: the Energy Minimization Multi-Scale Method*. Metallurgical Industry Press, Beijing.
- Liu, Y., Chen, J., Ge, W., Wang, J., Wang, W., 2011. Acceleration of CFD simulation of gas-solid flow by coupling macro-/meso-scale EMMS model. *Powder Technol.* 212, 289–295.
- Lu, B., Wang, W., Li, J., 2009. Searching for a mesh-independent sub-grid model for CFD simulation of gas-solid riser flows. *Chem. Eng. Sci.* 64, 3437–3447.
- Lu, B., Zhang, N., Wang, W., Li, J., Chiu, J.H., Kang, S.G., 2013. 3-D full-loop simulation of an industrial-scale circulating fluidized-bed boiler. *AIChE J.* 59, 1108–1117.
- O'Brien, T. J., Syamlal, M., 1993. Particle cluster effects in the numerical simulation of a circulating fluidized bed. In: Avidan, A. A. (Ed.), Preprint Volume for CFB-IV, New York, pp. 4330–4435.
- Sakai, M., Koshizuka, S., 2009. Large-scale discrete element modeling in pneumatic conveying. *Chem. Eng. Sci.* 64, 533–539.
- Shi, Z., Wang, W., Li, J., 2011. A bubble-based EMMS model for gas-solid bubbling fluidization. *Chem. Eng. Sci.* 66, 5541–5555.
- Soundararajan, S., Dalai, A.K., Berruti, F., 2001. Modeling of methanol to olefins (MTO) process in a circulating fluidized bed reactor. *Fuel* 80, 1187–1197.
- Tian, P., Wei, Y., Ye, M., Liu, Z., 2015. Methanol to olefins (MTO): from fundamentals to commercialization. *ACS Catal.* 5, 1922–1938.
- Tong, J., Li, J., 1982. *Computation for Thermophysical Properties of Fluid* (In Chinese). Tsinghua University Press, Beijing.
- Wang, J., Zhou, Q., Hong, K., Wang, W., Li, J., 2012. An EMMS-based multi-fluid model (EFM) for heterogeneous gas-solid riser flows: part II. An alternative formulation from dominant mechanisms. *Chem. Eng. Sci.* 75, 349–358.
- Wang, W., Li, J., 2007. Simulation of gas-solid two-phase flow by a multi-scale CFD approach—extension of the EMMS model to the sub-grid level. *Chem. Eng. Sci.* 62, 208–231.
- Wu, D., He, K., 2015. Progresses in MTO and MTP process technology and industrial application. *Petrochem. Technol.* 44, 1–10.
- Yang, N., Wang, W., Ge, W., Li, J., 2003. CFD simulation of concurrent-up gas-solid flow in circulating fluidized beds with structure-dependent drag coefficient. *Chem. Eng. J.* 96, 71–80.
- Zhang, N., Lu, B., Wang, W., Li, J., 2010. 3D CFD simulation of hydrodynamics of a 150 MWe circulating fluidized bed boiler. *Chem. Eng. J.* 162, 821–828.
- Zhao, M., Lu, B., Wang, W., Huang, W., Li, J., 2013a. Influence of initial distributions on hydrodynamic simulation of gas-solids riser. *CIESC J.* 64, 811–817.
- Zhao, Y., Li, H., Ye, M., Liu, Z., 2013b. 3D numerical simulation of a large scale MTO fluidized bed reactor. *Ind. Eng. Chem. Res.* 52, 11354–11364.
- Zhuang, Y.-Q., Chen, X.-M., Luo, Z.-H., Xiao, J., 2014. CFD-DEM modeling of gas-solid flow and catalytic MTO reaction in a fluidized bed reactor. *Comput. Chem. Eng.* 60, 1–16.